

Higher-order topological corner states and origin in monolayer LaBrO

Qing Wang(王庆) and Ning Hao(郝宁)
Citation: Chin. Phys. B, 2024, 33 (**12**): 127303. DOI: 10.1088/1674-1056/ad8a50
Journal homepage: http://cpb.iphy.ac.cn; http://iopscience.iop.org/cpb

What follows is a list of articles you may be interested in

Strain-modulated antiferromagnetic Chern insulator in $NiOsCl_6$ monolayer

Bin Wu(武斌), Na Li(李娜), Xin-Lian Chen(陈新莲), Wei-Xiao Ji(纪维霄), Pei-Ji Wang(王培吉), Shu-Feng Zhang(张树峰), and Chang-Wen Zhang(张昌文)
Chin. Phys. B, 2024, 33 (**12**): 127301. DOI: 10.1088/1674-1056/ad84cb

$GaInX_3$ (X = S, Se, Te): Ultra-low thermal conductivity and excellent thermoelectric performance

Zhi-Fu Duan(段志福), Chang-Hao Ding(丁长浩), Zhong-Ke Ding(丁中科), Wei-Hua Xiao(肖威华), Fang Xie(谢芳), Nan-Nan Luo(罗南南), Jiang Zeng(曾犟), Li-Ming Tang(唐黎明), and Ke-Qiu Chen(陈克求)
Chin. Phys. B, 2024, 33 (**8**): 087302. DOI: 10.1088/1674-1056/ad47e3

Intrinsic valley-polarized quantum anomalous Hall effect in a two-dimensional germanene/MnI_2 van der Waals heterostructure

Xiao-Jing Dong(董晓晶) and Chang-Wen Zhang(张昌文)
Chin. Phys. B, 2024, 33 (**7**): 077303. DOI: 10.1088/1674-1056/ad4bbd

Effect of strain on structure and electronic properties of monolayer C_4N_4

Hao Chen(陈昊), Ying Xu(徐瑛), Jia-Shi Zhao(赵家石), and Dan Zhou(周丹)
Chin. Phys. B, 2024, 33 (**5**): 057302. DOI: 10.1088/1674-1056/ad260c

Machine learning of the Γ-point gap and flat bands of twisted bilayer graphene at arbitrary angles

Xiaoyi Ma(马宵怡), Yufeng Luo(罗宇峰), Mengke Li(李梦可), Wenyan Jiao(焦文艳), Hongmei Yuan(袁红梅), Huijun Liu(刘惠军), and Ying Fang(方颖)
Chin. Phys. B, 2023, 32 (**5**): 057306. DOI: 10.1088/1674-1056/acb2c3

RAPID COMMUNICATION

Higher-order topological corner states and origin in monolayer LaBrO

Qing Wang(王庆)[1,2] and Ning Hao(郝宁)[1,†]

[1] *Anhui Province Key Laboratory of Low-Energy Quantum Materials and Devices, High Magnetic Field Laboratory, HFIPS, Anhui, Chinese Academy of Sciences, Hefei* 230031, *China*

[2] *Science Island Branch of Graduate School, University of Science and Technology of China, Hefei* 230026, *China*

(Received 29 September 2024; revised manuscript received 22 October 2024; accepted manuscript online 23 October 2024)

Intrinsic higher-order topological insulators driven solely by orbital coupling are rare in electronic materials. Here, we propose that monolayer LaBrO is an intrinsic two-dimensional second-order topological insulator. The generalized second-order topological phase arises from the coupling between the 5d orbital of the La atom and the 2p orbital of the O atom. The underlying physics can be thoroughly described by a four-band generalized higher-order topological model. Notably, the edge states and corner states of monolayer LaBrO exhibit different characteristics in terms of morphology, number, and location distribution under different boundary and nanocluster configurations. Furthermore, the higher-order topological corner states of monolayer LaBrO are robust against variations in spin–orbit coupling and different values of Hubbard U. This provides a material platform for studying intrinsic 2D second-order topological insulators.

Keywords: second order topological insulator, first-principles calculations, higher order topological model, zero-dimensional corner state

PACS: 73.22.–f, 31.15.es, 73.20.At, 02.40.–k **DOI:** 10.1088/1674-1056/ad8a50

1. Introduction

In recent years, higher-order topological states have attracted significant attention.[1–14] Different from the traditional first-order topology,[15–19] the generalized bulk–boundary correspondence in higher-order topology involves a larger dimensional difference. Among these, two-dimensional second-order topological insulators (SOTI) are the simplest, featuring zero-dimensional topological corner states. A substantial class of higher-order topologies is driven by spin–orbit coupling (SOC), which can be viewed as the introduction of edge state coupling terms based on the first-order topology. This can occur in systems with factors such as in-plane Zeeman fields,[10] magnetic heterojunctions,[20] and ferroelectric switches,[21] leading the system to enter a higher-order topological phase. However, the band gap of such higher-order topological insulators driven by SOC is typically small, posing considerable challenges for experimental observation. Another major class of higher-order topological insulators is intrinsic higher-order topology,[1,22–24] which does not rely on SOC and can be observed in spinless systems with a bulk band gap of several electron Volts. The most notable example is the quadrupole higher-order topological insulator described by the Benalcazar–Bernevig–Hughes (BBH) model.[1]

Since the concept of higher order topology was proposed, relevant theoretical predictions and experimental studies have also developed rapidly in the field of condensed matter physics, such as magic-angle graphene[1,25,26] and γ-graphyne.[27] In magnetic systems, magnetic higher-order topological insulators can emerge in heterostructures like EuO/Bi[20] and $CoBr_2/Pt_2HgSe_3/CoBr_2$.[28] Notably, spin-dependent SOTI has been identified in antiferromagnetic FeSe/GdClO heterostructure.[29] Furthermore, the existence of higher-order topological corner states can be observed in large band gaps that are not induced by SOC in many non-dimerized ordinary lattice materials. This phenomenon can be understood and characterized by the theoretical model we proposed in our previous work[30] for such higher-order topological insulator materials. For instance, the material BaHCl, which has a tetragonal structure, is analogous to that of the iron-based superconductor family.

In this paper, we demonstrate through first-principles calculations that monolayer LaBrO is an intrinsic two-dimensional SOTI, which is characterized by the emergence of nontrivial higher-order topological corner states. The origin of this higher-order topology arises from the interaction between the 5d orbitals of La atoms and the 2p orbitals of O atoms. This interaction can be fully described by a four-band model that perfectly corresponds to the primitive cell of monolayer LaBrO. Furthermore, by constructing a $\sqrt{2}\times\sqrt{2}$ supercell, we observe edge states associated with another type of boundary, as well as the corner states of the resulting nanocluster. Notably, our calculations indicate that the predicted corner states of monolayer LaBrO, which carry the intrinsic two-dimensional SOTI property, are robust and independent

†Corresponding author. E-mail: haon@hmfl.ac.cn

© 2024 Chinese Physical Society and IOP Publishing Ltd

of SOC and varying values of Hubbard U. This makes LaBrO an ideal material for observing such intrinsic two-dimensional SOTI.

2. Computational details

Based on density functional theory (DFT), first-principles calculations were carried out using the Vienna *Ab initio* Simulation Package (VASP).[31] The generalized gradient approximation (GGA) developed by the Perdew–Burke–Ernzerhof functional (PBE)[32] was employed for the exchange–correlation potential. A vacuum layer of 25 Å was used to ensure decoupling between neighboring slabs, and the cutoff energy was fixed at 520 eV. All atoms were fully relaxed until the forces on each atom were smaller than 0.001 eV/Å during the structural relaxation of monolayer LaBrO. The Brillouin zone (BZ) sampling was performed using Γ-centered Monkhorst–Pack grids with an $11 \times 11 \times 1$ mesh for atomic geometry optimization and self-consistent calculations. Phonon calculations were conducted utilizing DFT perturbation theory with phonopy packages.[33] We adopted the PBE $+U$ calculation method to deal with the strong correlation effects for the 4f-orbitals of La, using $U_{\text{eff}} = 5$ eV for the final corner states stability verification of monolayer LaBrO.[34] The tight-binding Hamiltonian, constructed from maximally localized Wannier functions that utilize results from first-principles calculations of monolayer LaBrO, was derived from band fitting using the Wannier90 package.[35]

3. Results and discussion

LaBrO is a ternary rare-earth metal oxyhalide with a space group of $P4/nmm$ (129).[36–39] Figure 1(a) illustrates the lattice structure of monolayer LaBrO, with the black boxes representing the primitive cells. Each primitive cell contains six atoms: two O atoms at the center and two Br atoms positioned at the outermost layers, resulting in a five-layer structure arranged in the sequence of Br–La–O–La–Br. The experimentally measured lattice constants of LaBrO are $a = b =$ 4.14 Å and $c = 7.39$ Å.[36] Along the c-axis, each layer of primitive cells is weakly connected by van der Waals forces, which makes LaBrO a naturally occurring two-dimensional material. The optimized lattice parameters for a monolayer of LaBrO are $a = b = 4.14$ Å, consistent with the experimental values for the bulk material.[36] As shown in Fig. 1(d), to confirm the stability of monolayer LaBrO, we calculated the corresponding phonon spectrum, and the results indicate the absence of imaginary frequencies throughout the Brillouin zone.

Figure 1(e) displays the orbital-projected band structure of monolayer LaBrO without considering SOC. It is evident that near the Fermi level, the valence band is primarily contributed by the 4p orbitals of Br atoms and the 2p orbitals of O atoms, while the conduction band is mainly composed of the 5d and 4f orbitals of La atoms. A large band gap of approximately 4 eV exists between the conduction and valence bands. Notably, both the valence band maximum (VBM) and the conduction band minimum (CBM) are located at the Γ point, indicative of a direct-gap insulator.

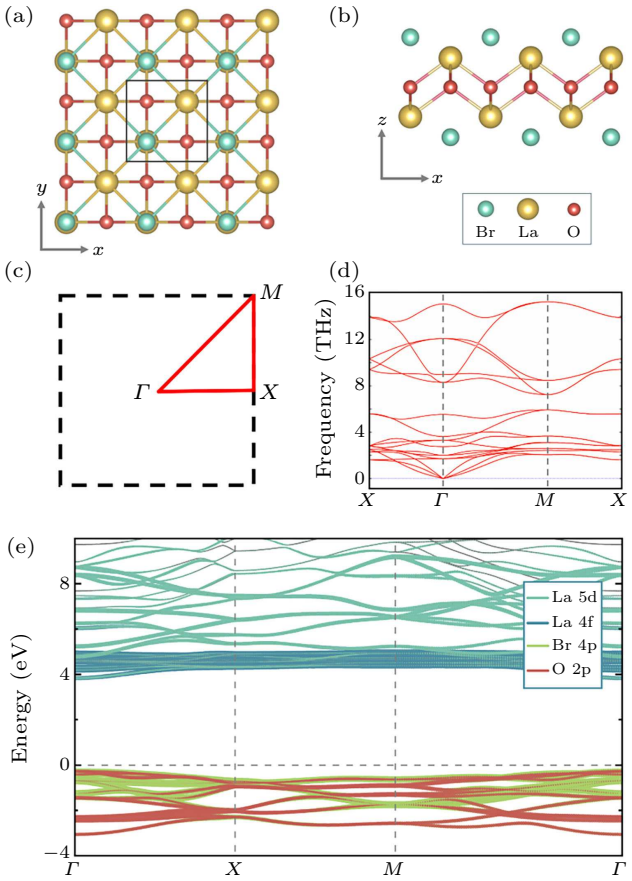


Fig. 1. The crystal structure of LaBrO: (a) top view and (b) side view. The unit cell of LaBrO is indicated by black solid lines. (c) The Brillouin zone of the primitive unit cell of monolayer LaBrO. (d) Phonon spectrum for monolayer LaBrO, indicating that the monolayer LaBrO is dynamically stable. (e) The orbital-projected band structure of monolayer LaBrO without considering SOC. The Fermi level is indicated with a dashed line.

Through semi-infinite edge spectral calculations, we observe edge states at the top of the bulk valence band, as presented in the edge spectrum in Fig. 2(a). At the Γ point, the edge states slightly embed into the bulk states. Subsequently, we constructed a square nanocluster consisting of 20×20 unit cells. The overall structure of this square nanocluster is shown in Fig. 1(a). The four boundaries are connected through rotational symmetry, making them all equivalent. However, the four corners display two distinct configurations: the upper left and lower right corners are occupied by O atoms, while the lower left and upper right corners are occupied by La and Br atoms at different heights. In the discrete energy spectrum of the square nanocluster, shown in Fig. 2(b), a pair of degenerate isolated states is clearly visible in the lower half of the bandgap. Notably, an analysis of the wave functions of these

isolated states reveals that they are localized at the corners of the nanocluster, as illustrated in the inset. This localization confirms the emergence of corner states in the SOTI phase.

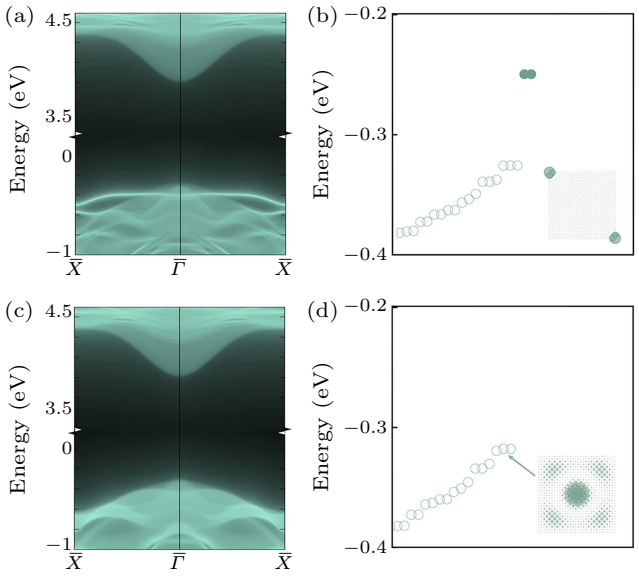


Fig. 2. (a) The semi-infinite edge spectrum of monolayer LaBrO with complete orbitals. (b) The discrete energy spectrum of the square nanocluster of monolayer LaBrO with complete orbitals. (c) The semi-infinite edge spectrum of monolayer LaBrO without 5d orbitals of La atoms. (d) The discrete energy spectrum of the square nanocluster of monolayer LaBrO without 5d orbitals of La atoms.

To further explore the specific origin of the SOTI corner states in monolayer LaBrO, we shift our focus back to the orbital composition. It is undeniable that the emergence of SOTI corner states stems from the interaction between the valence and conduction bands. Regarding the valence band, the entanglement of the p orbitals of Br atoms and the p orbitals of O atoms in the bands below the Fermi level complicates the identification of the origin of the second-order topology through edge spectrum and discrete energy spectrum of the square nanocluster analysis alone. Fortunately, as shown in the illustration in Fig. 2(b), the spatial distribution of the corner state wavefunctions reveals that the two degenerate corner states are localized on the O atoms located at the upper left and lower right corners of the nanocluster. This directly suggests that the 2p orbitals of O atoms in the valence band play a crucial role in forming the SOTI phase of the system.

For the conduction band, we cannot replicate this method to distinguish between the 5d and 4f orbitals of the same atom. Therefore, we adopt an alternative approach. We construct a system that excludes the 5d orbitals of La atoms while keeping everything else identical, as shown in Figs. 2(c) and 2(d). By performing identical calculations on both the semi-infinite edge spectrum and the discrete energy spectrum of the square nanocluster, we observe that the corresponding topological boundary states and higher-order topological corner states disappear, rendering the system trivial. This indicates that the generalized second-order topological phase hosted in monolayer LaBrO arises from the coupling between the 5d orbitals of La atoms and the 2p orbitals of O atoms. This finding is also consistent with the general consensus that 4f orbitals are typically more localized.

Through the analysis of the energy and spatial distribution of higher-order topological corner states in monolayer LaBrO nanoclusters, we discovered that the higher-order topological phase exhibited by this system can be accurately described by the generalized higher-order topological model we previously proposed.[30] By rotating the two-dimensional checkerboard lattice in this model by 45°, we obtain a lattice that is completely equivalent to the primitive cell of monolayer LaBrO. In this configuration, the primitive cell encompasses four sublattices. Since monolayer LaBrO is a non-magnetic material, spin does not need to be considered in the model. The transformed four-band Hamiltonian can be expressed as

$$H=\begin{pmatrix} h_{\mathrm{E}} & \nu+\mathrm{e}^{-\mathrm{i}k_x}\nu & \nu+\mathrm{e}^{-\mathrm{i}k_y}\nu & A_1 \\ & -h_{\mathrm{E}} & A_2 & \nu+\mathrm{e}^{-\mathrm{i}k_y}\nu \\ & & -h_{\mathrm{E}} & \nu+\mathrm{e}^{-\mathrm{i}k_x}\nu \\ \text{H.c.} & & & h_{\mathrm{E}} \end{pmatrix}, \tag{1}$$

with

$$\begin{aligned} h_{\mathrm{E}} &= e+2t\cos(k_x)+2t\cos(k_y), \\ A_1 &= t_1(1+\mathrm{e}^{-\mathrm{i}k_x}+\mathrm{e}^{-\mathrm{i}k_y}+\mathrm{e}^{-\mathrm{i}(k_x+k_y)}), \\ A_2 &= -t_1(1+\mathrm{e}^{\mathrm{i}k_x}+\mathrm{e}^{-\mathrm{i}k_y}+\mathrm{e}^{\mathrm{i}(k_x-k_y)}). \end{aligned} \tag{2}$$

Here, e represents the on-site energy of the orbital, ν denotes nearest-neighbor hopping, t_1 represents next-nearest-neighbor hopping, and t represents next-next-nearest-neighbor hopping. the basis functions of Hamiltonian in Eq. (1) can be defined as $\psi(k)=[d_{\mathrm{La1}}(k),p_{\mathrm{O1}}(k),p_{\mathrm{O2}}(k),d_{\mathrm{La2}}(k)]^{\mathrm{T}}$. When the parameters of the system satisfy

$$\begin{cases} -\left[4(t+t_1)+\frac{4\nu^2}{2t+t_1}\right]<e<4t, & t>0, \\ 4t<e<-\left[4(t+t_1)+\frac{4\nu^2}{2t+t_1}\right], & t<0, \end{cases} \tag{3}$$

the system enters a generalized SOTI phase, characterized by a pair of opposite projected winding numbers[30] $W^{\pm}_{\mathrm{2D,P}}=\pm1$. In Fig. 3, we have plotted the corresponding edge spectrum and the discrete energy spectrum of the square nanocluster of the model within this phase. The shaded area represents the trivial bulk states in the material, indicating that the edge and corner states located in the upper half of the Fermi level in monolayer LaBrO are submerged in the bulk states and therefore cannot be observed. Meanwhile, the number and positions of the corner states appearing in the lower half of the Fermi level of the model are fully consistent with those in the monolayer LaBrO.

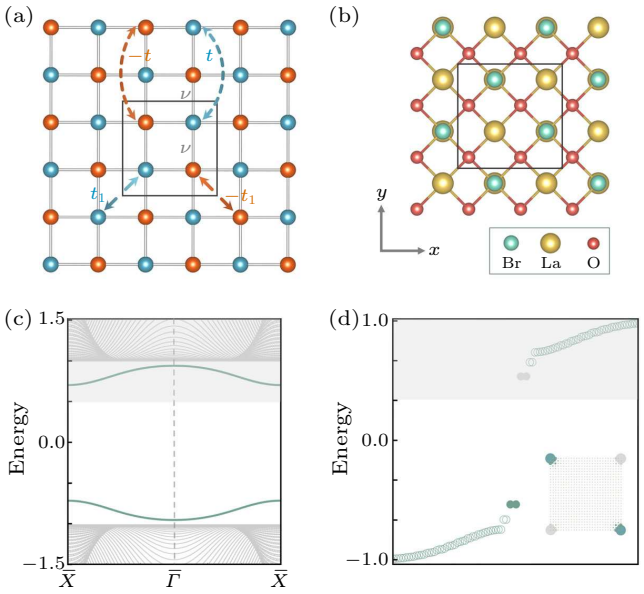


Fig. 3. (a) Lattice diagram of a four-band generalized higher-order topological model, created by rotating the two-dimensional checkerboard lattice by 45°. Not all hoppings are shown for clarity. (b) Diagram of the structure of a square nanocluster consisting of $\sqrt{2}\times\sqrt{2}$ supercells of monolayer LaBrO. The solid black line frame represents the unit cell of the supercell. (c) The edge spectrum of the theoretical model. (d) The discrete energy spectrum of the square nanocluster based on the theoretical model. The parameters are $\nu = t_1 = 1$, $t = 0.5$, and $e = 1$.

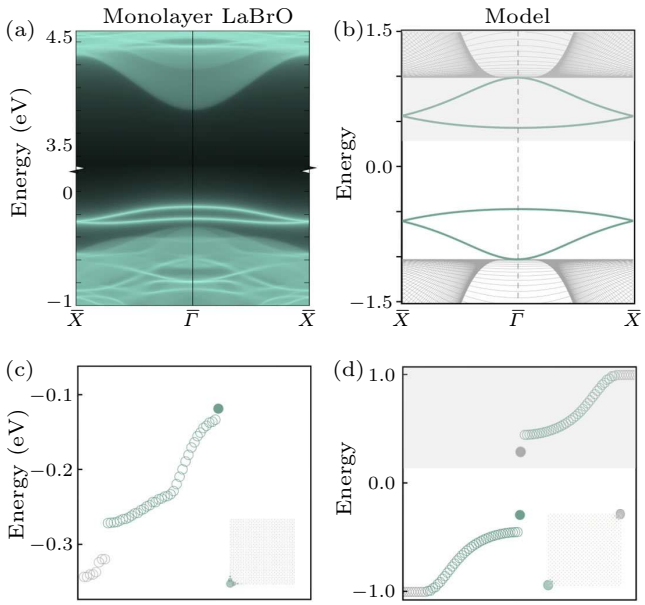


Fig. 4. (a) The edge spectrum and (c) corresponding discrete energy spectrum of the square nanocluster under the new boundary configuration within the monolayer LaBrO supercell with $\sqrt{2}\times\sqrt{2}$ size. (b) The edge spectrum after folding the Brillouin zone and (d) corresponding discrete energy spectrum of the square nanocluster under the new boundary configuration within the two-band checkerboard lattice theoretical model. The parameters are $\nu = t_1 = 1$, $t = 0.5$, and $e = 1$.

In addition, as shown in Fig. 3(b), a monolayer LaBrO supercell with $\sqrt{2}\times\sqrt{2}$ size is constructed. The edge spectrum and the discrete energy spectrum of the square nanocluster of this supercell and the two-band checkerboard lattice model are calculated as additional evidence and supplements. As shown in Fig. 4, the theoretical model and monolayer LaBrO yield identical results. The boundary of the O atom in this configuration disrupts more hopping terms with the La atom, making the edge state in the edge spectrum more prominent than that of the previous primitive cell configuration. Additionally, the number of edge states changes. Two edge states are observed in Fig. 4(a), where they degenerate at the boundary of the one-dimensional Brillouin zone. This degeneracy occurs because the original Brillouin zone of the primitive cell is folded accordingly, with the fold becoming the boundary of the new Brillouin zone. Thus, the two edge states are effectively a single entity. However, in the square nanoclusters with this structure, as shown in Fig. 3(b), only the corner occupied by O atoms in the lower left corner and the corner occupied by La atoms in the upper right corner can truly contain isolated atoms. Consequently, as shown in Figs. 4(c) and 4(d), the number of corner states in the lower half of the Fermi level in the discrete energy spectrum of the nanoclusters is limited to one, with its wave function localized on the isolated O atom in the lower left corner.

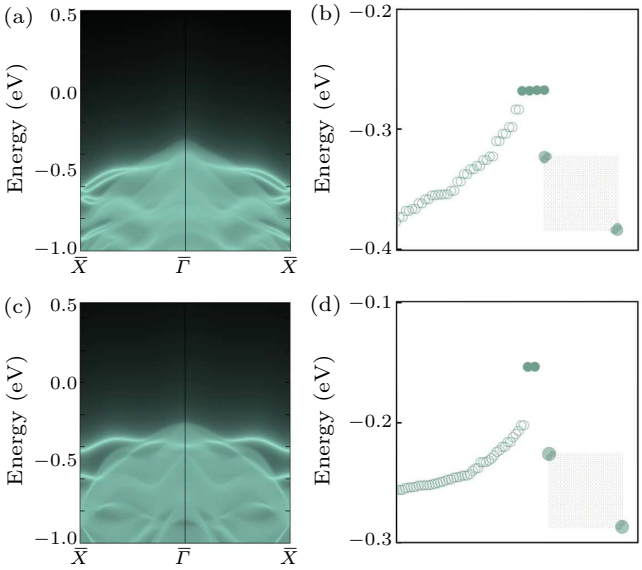


Fig. 5. (a) The edge spectrum and (b) discrete energy spectrum of the square nanocluster of monolayer LaBrO under SOC are considered. (c) The edge spectrum and (d) discrete energy spectrum of the square nanocluster of monolayer LaBrO under strong correlation effects are considered. We use $U_{\text{eff}} = 5$ eV to verify the stability of the final corner states in monolayer LaBrO.

The intrinsic higher-order topological corner states, which are solely driven by orbital coupling, are inherently robust and particularly immune to SOC. To verify this, we calculated the relevant results for monolayer LaBrO after incorporating SOC, as shown in Figs. 5(a) and 5(b). In the edge energy spectrum, the edge states double due to the increase in spin degree of freedom. Similarly, in the discrete energy spectrum of the square nanocluster, four corner states localized at the corners of two O atoms can be observed. Furthermore, to demonstrate the reliability of our theoretical predictions and their independence from certain empirical parameters, we validated the stability of the higher-order topological corner states

in monolayer LaBrO by varying the U values, as depicted in Figs. 5(c) and 5(d). The results indicate that both the edge states and corner states of the system remain stable.

4. Conclusion

Thus far, through first-principles calculations, we have demonstrated that monolayer LaBrO is an intrinsic two-dimensional second-order topological insulator, characterized by the emergence of nontrivial higher-order topological corner states. We have explained and verified that the generalized second-order topological phase in monolayer LaBrO arises from the coupling between the 5d orbitals of La atoms and the 2p orbitals of O atoms. A four-band tight-binding model is employed to describe the origin and physical mechanism of this generalized second-order topology. The precise correspondence between the number and spatial distribution of edge and corner states in monolayer LaBrO and the theoretical model across different boundary configurations and nanoclusters effectively explains the various higher-order topological phenomena observed in monolayer LaBrO, while also validating the accuracy of the model. Our research results indicate that monolayer LaBrO is one of the ideal materials for studying such intrinsic two-dimensional second-order topological insulators.

Acknowledgments

This work was financially supported by the National Key R&D Program of China (Grant No. 2022YFA1403200), the National Natural Science Foundation of China (Grant Nos. 92265104, 12022413, and 11674331), the Basic Research Program of the Chinese Academy of Sciences Based on Major Scientific Infrastructures (Grant No. JZHKYPT-2021-08), the CASHIPS Director's Fund (Grant No. BJPY2023A09), the "Strategic Priority Research Program (B)" of the Chinese Academy of Sciences (Grant No. XDB33030100), Anhui Provincial Major S&T Project (Grant No. s202305a12020005), the Major Basic Program of Natural Science Foundation of Shandong Province (Grant No. ZR2021ZD01), and the High Magnetic Field Laboratory of Anhui Province (Grant No. AHHM-FX-2020-02).

References

[1] Benalcazar W A, Bernevig B A and Hughes T L 2017 *Science* **357** 61
[2] Benalcazar W A, Bernevig B A and Hughes T L 2017 *Phys. Rev. B* **96** 245115
[3] Schindler F, Cook A M, Vergniory M G, Wang Z, Parkin S S P, Bernevig B A and Neupert T 2018 *Sci. Adv.* **4** eaat0346
[4] Song Z, Fang Z and Fang C 2017 *Phys. Rev. Lett.* **119** 246402
[5] Geier M, Trifunovic L, Hoskam M and Brouwer P W 2018 *Phys. Rev. B* **97** 205135
[6] Khalaf E 2018 *Phys. Rev. B* **97** 205136
[7] van Miert G and Ortix C 2018 *Phys. Rev. B* **98** 081110
[8] Călugăru D, Juričić V and Roy B 2019 *Phys. Rev. B* **99** 041301
[9] Sheng X L, Chen C, Liu H, Chen Z, Yu Z M, Zhao Y X and Yang S A 2019 *Phys. Rev. Lett.* **123** 256402
[10] Ren Y, Qiao Z and Niu Q 2020 *Phys. Rev. Lett.* **124** 166804
[11] Liu B, Xian L, Mu H, Zhao G, Liu Z, Rubio A and Wang Z F 2021 *Phys. Rev. Lett.* **126** 066401
[12] Liao M J, Wei M S, Wang S, Xu J and Yang Y 2024 *Chin. Phys. B* **33** 060305
[13] Han B, Zeng J and Qiao Z 2022 *Chin. Phys. Lett.* **39** 017302
[14] Shen Y F, Xu X F, Sun M, Zhou W J and Chang Y J 2024 *Chin. Phys. B* **33** 044203
[15] Hasan M Z and Kane C L 2010 *Rev. Mod. Phys.* **82** 3045
[16] Qi X L and Zhang S C 2011 *Rev. Mod. Phys.* **83** 1057
[17] Kane C L and Mele E J 2005 *Phys. Rev. Lett.* **95** 226801
[18] Bernevig B A, Hughes T L and Zhang S C 2006 *Science* **314** 1757
[19] Bansil A, Lin H and Das T 2016 *Rev. Mod. Phys.* **88** 021004
[20] Chen C, Song Z, Zhao J Z, Chen Z, Yu Z M, Sheng X L and Yang S A 2020 *Phys. Rev. Lett.* **125** 056402
[21] Li R, Mao N, Cai L, Bai Y, Huang B, Dai Y and Niu C 2023 *Phys. Rev. B* **108** 125302
[22] Liu F and Wakabayashi K 2017 *Phys. Rev. Lett.* **118** 076803
[23] Luo X J, Pan X H, Liu C X and Liu X 2023 *Phys. Rev. B* **107** 045118
[24] Götz A, Hohenadler M and Assaad F F 2024 *Phys. Rev. B* **109** 195154
[25] Ma C, Wang Q, Mills S, Chen X, Deng B, Yuan S, Li C, Watanabe K, Taniguchi T, Du X, *et al.* 2020 *Nano Lett.* **20** 6076
[26] Park M J, Kim Y, Cho G Y and Lee S 2019 *Phys. Rev. Lett.* **123** 216803
[27] Liu B, Zhao G, Liu Z and Wang Z F 2019 *Nano Lett.* **19** 6492
[28] Liu Z, Ren Y, Han Y, Niu Q and Qiao Z 2022 *Phys. Rev. B* **106** 195303
[29] Wang Q, Song R and Hao N 2023 *Phys. Rev. B* **107** 235406
[30] Wang Q and Hao N 2024 arXiv:2407.00795
[31] Kresse G and Furthmüller J 1996 *Phys. Rev. B* **54** 11169
[32] Perdew J P, Burke K and Ernzerhof M 1996 *Phys. Rev. Lett.* **77** 3865
[33] Togo A and Tanaka I 2015 *Scripta Materialia* **108** 1
[34] Dudarev S L, Botton G A, Savrasov S Y, Humphreys C J and Sutton A P 1998 *Phys. Rev. B* **57** 1505
[35] Mostofi A A, Yates J R, Pizzi G, Lee Y S, Souza I, Vanderbilt D and Marzari N 2014 *Comput. Phys. Commun.* **185** 2309
[36] Sillen L 1941 *Sven. Kem. Tidskr.* **53** 367
[37] Brixner L and Moore E 1983 *Acta Cryst.* **39** 1316
[38] Limburg H J, Hölsä J, Porcher P, Herzog G, Starick D and Wulff H 1992 *J. Solid State Chem.* **98** 404
[39] Haeuseler H and Jung M 1986 *Mater. Res. Bull.* **21** 1291